



저작자표시-비영리-변경금지 2.0 대한민국

이용자는 아래의 조건을 따르는 경우에 한하여 자유롭게

- 이 저작물을 복제, 배포, 전송, 전시, 공연 및 방송할 수 있습니다.

다음과 같은 조건을 따라야 합니다:



저작자표시. 귀하는 원저작자를 표시하여야 합니다.



비영리. 귀하는 이 저작물을 영리 목적으로 이용할 수 없습니다.



변경금지. 귀하는 이 저작물을 개작, 변형 또는 가공할 수 없습니다.

- 귀하는, 이 저작물의 재이용이나 배포의 경우, 이 저작물에 적용된 이용허락조건을 명확하게 나타내어야 합니다.
- 저작권자로부터 별도의 허가를 받으면 이러한 조건들은 적용되지 않습니다.

저작권법에 따른 이용자의 권리는 위의 내용에 의하여 영향을 받지 않습니다.

이것은 [이용허락규약\(Legal Code\)](#)을 이해하기 쉽게 요약한 것입니다.

[Disclaimer](#)

Thesis for the Degree of Master of Engineering

**Cloud detection in the sun-glint region
using the analysis
of Specular reflection pattern**



by

Chaeyoung Kwon

Department of Spatial Information Engineering

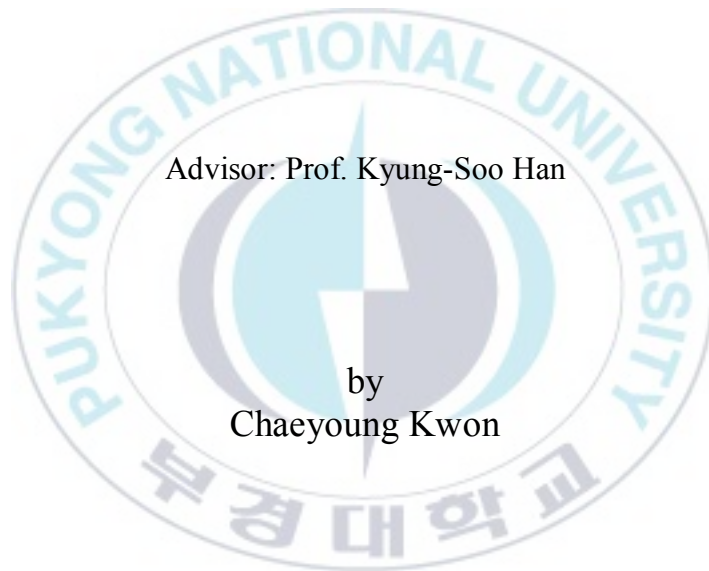
The Graduate School

Pukyong National University

February 2018

**Cloud detection in the sun-glint region
using the analysis
of Specular reflection pattern**

태양광 정반사 반사 패턴 분석을 활용한
sun-glint 영역에서의 구름탐지



Advisor: Prof. Kyung-Soo Han

by
Chaeyoung Kwon

thesis submitted in partial fulfillment of the requirements
for the degree of Master of Engineering
in Department of Spatial Information Engineering,
The Graduate School,
Pukyong National University

February 2018

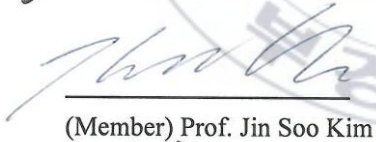
**Cloud detection in the sun-glint region using the analysis
Of Specular reflection pattern**

A dissertation
by
Chaeyoung Kwon

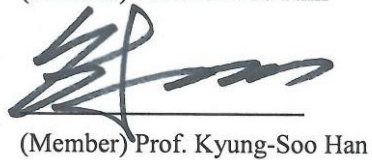
Approved by:



(Chairman) Prof. Han Rim Lee



(Member) Prof. Jin Soo Kim



(Member) Prof. Kyung-Soo Han

February. 23, 2018

CONTENTS

CONTENTS	i
TABLE OF CONTENTS.....	iii
LIST OF FIGURES	iv
LIST OF ACRONYMS	vii
1. Introduction	1
1.1. Background	1
1.1.1. Sun-glnt phenomenon	1
1.1.2. Cloud detection.....	5
1.1.3. Cloud detection in sun-glnt	7
2. Data and Materials	9
2.1. Himawari-8/AHI.....	9
2.2. Cloud mask of NOAA	12
2.3. JMA cloud type data	13
3. Methodology and Results	15
3.1. Synthetic Methodology.....	15
3.2. Reflectance Normalization.....	17
3.3. Sun-glnt detection.....	18
3.3.1. Sun-glnt detection	18
3.4. Construction of ocean spectral reflectance library	20
3.5. Dynamic Wavelength Warping (DWW)	22
3.5.1. Dynamic Time Warping (DTW).....	22
3.5.2. Dynamic Wavelength Warping (DWW).....	24
3.6. IST0 method	27

4. Evaluation	30
4.1. Evaluation of result of cloud detection using DWW	30
4.2. Evaluation of result of cloud detection using ISTO	36
4.3. Qualitative validation with AHI cloud type of JMA and AHI SST quality flag of NOAA.....	38
5. Summary and Conclusions.....	44
6. References	45



TABLE OF CONTENTS

Table 1 two concepts of the glint correction method, and it can be categorized by method principle	4
Table 2 Himawari-8/AHI specifications	11
Table 3 JMA cloud type (ISCCP Definition)	14
Table 4 Case classification of RGB true color image and cloud mask from NOAA, JMA and our result	35
Table 5 Information about SZA, VZA, Total cumulative smallest cost in each case	35

LIST OF FIGURES

Figure 1 Study area - full disk of himawari-8/AHI.....	10
Figure 2 flow chart of this study.....	16
Figure 3 Sun-glint area in AHI's full disk disk as a function of glint angle(θ_g) and the threshold value is 40° (a) 2016/08/17 08:00 UTC (b) 2016/08/17 03:00 UTC (c) 2016/08/17 21:00 UTC (d) 2016/08/17 19:00 UTC (e) 2016/08/17 18:00 UTC (f) 2016/08/17 17:00 UTC.....	19
Figure 4 ocean spectral reflectance library depending change of SZA and VZA.....	21
Figure 5 To find the optimal warping path, we construct a Cost matrix using Dynamic Time Warping (DTW) method.....	26
Figure 6 spatial distribution of weekly sea ice of National Snow and Ice Data Center (NSIDC) during Northern hemisphere winter season (from December to February) from 1980 to 2015	29

Figure 7 (a) is total cumulative smallest cost value, (b) is red-green-blue (RGB) composite image and (c) is detected area that total cumulative smallest cost value larger than 0.6 at region of sun-glint acquired at 03:00 UTC 1 August 2016 31

Figure 8 plotted reflectance profile observed and selected reflectance profile from ocean spectral reflectance library under SZA and VZA condition at the time of observation 34

Figure 9. A case from 0300 UTC on 1 August 2016. (a) sky blue is cloud detection result when total cumulative smallest cost is greater than 0.6 and orange is cloud detection result when **ISTO** – 11.2 μm channel BT is greater than -15 K (b) RGB composite image..... 37

Figure 10 visual comparison with true color RGB image, AHI cloud type of JMA and our cloud detection result at 0100 UTC 1 August 2016 40

Figure 11 visual comparison with true color RGB image, AHI SST quality flag of NOAA and our cloud detection result at 0100 UTC 1 August 2016 41

Figure 12 visual comparison with true color RGB image, AHI cloud type
of JMA and our cloud detection result at 0200 UTC 3 August 2016
..... 42

Figure 13 visual comparison with true color RGB image, AHI SST quality
flag of NOAA and our cloud detection result at 0200 UTC 3 August
2016 43



LIST OF ACRONYMS



ACSP0	Advanced Clear-Sky Processor for Oceans
AHI	Advanced Himawari Imager
BTD	Brightness Temperature Difference
CZCS	Coastal Zone Colour Scanner
DTW	Dynamic Time Warping
DWW	Dynamic Wavelength Warping
iQuam	in-situ SST Quality Monitor
ISCCP	International Satellite Cloud Climatology Project
JMA	Japan Meteorological Agency
MODIS	Moderate Resolution Imaging Spectroradiometer
MTSAT-2	Multifunctional Transport Satellite – 2
NOAA	National Oceanic and Atmospheric Administration
RAA	Relative Azimuth Angle
SeaWiFS	Sea-viewing Wide Field-of-view Sensor
SNR	Signal to Noise Ratio
S-NPP	Suomi-National Polar-orbiting Partnership
SST	Sea Surface Temperature

SZA	Solar Zenith Angle
VIIRS	Visible–Infrared Imager–Radiometer Suite
VZA	Viewing Zenith Angle



태양광 정반사 반사 패턴 분석을 활용한 sun-glint 영역에서의 구름 탐지

권 채 영

부 경 대 학 교 대 학 원 공 간 정 보 시 스템 공 학 전 공

요 약

Sun-glint란 정반사(specular reflection)된 반사광이 위성 센서의 시야각 (field of view) 범위 내에 존재하여 위성영상에서 나타날 때를 의미하며, 대부분 해양에서 발생한다. 이러한 sun-glint 영향을 받은 화소에서는 구름과 청천 모두 높은 대기 상한 반사도를 보여 청천 화소에서 구름과의 오탐지가 나타나기 쉽다. 또한, 위성 영상의 정확한 구름 판별 여부는 이를 활용하여 생산되는 다른 산출물들의 정확도에 민감한 영향을 미치므로 매우 중요하다. 따라서 본 연구에서는 Himawari-8 위성의 Advanced Himawari Imager (AHI) 센서의 관측 영역에서 태양 천정각 (Solar Zenith Angle: SZA), 위성 천정각 (Viewing Zenith Angle: VZA), 상대 방위각 (Relative Azimuth Angle: RAA)의 변화에 따라 sun-glint 지역을 지정하고 지정된 지역에 한하여 구름탐지를 수행하였다. 구름탐지에 앞서 청천 화소의 분광 특성을 분석하기 위하여 태양 천정각 및 위성 천정각 변화에 따른 청천 해양 표면 화소의 반사도를 수집하여 분광 라이브러리를 구축하였다. 청천 해양 표면 분광 라이브러리 구축 결과, Sun-glint 영역에서 반사도는 일정한 분광 패턴을 가지고 있었으며 이를 이용하여 패턴 인식 기법인 Dynamic Wavelength Warping (DWW) 기법에 적용하여 구름탐지를 수행하였다. 본 연구의 구름탐지 결과를 Japan Meteorological Agency (JMA)의 AHI cloud type 자료와 National Oceanic and Atmospheric Administration (NOAA)의 Advanced Clear-Sky Processor for Ocean (ACSP)의 Sea surface temperature (SST) 시스템의 AHI SST의 Quality Flag를 RGB 합성영상을 통하여 정성적 비교 및 검증 실시하였다. 그 결과, JMA 구름 산출물은 Sun-glint 영향이 강하게 나타나 RGB 합성영상에서 밝게 빛나는 지역에서 청천 화소를 구름으로 오탐지하는 경향을 보였으며 NOAA의 AHI SST Quality Flag는 sun-glint 영역에서

구름을 전체적으로 오탐지하는 경향을 보였다. 그러나 본 연구에서는 이러한 오탐지 경향을 개선하였으며 RGB 합성영상의 구름 분포와 유사한 결과를 보였다.



1. Introduction

1.1. Background

1.1.1. Sun-glint phenomenon

Sun-glint occurs in imagery when the sun light directly reflected towards the sensor over the sea surface known as specular reflection. Sun-glint is a serious error factor for remote sensing of the ocean and atmosphere optical properties (e.g., aerosol optical thickness, ocean color) and water column properties and benthos (*Wang and bailey 2001, Hedley et al 2005, Kay et al. 2009, Ignatov et al. 2005*). Hochberg *et al.* (2003) reported that accuracy of estimation of near-shore environments was less precise at critical benthic habitat by uncorrected glint. Goodman *et al.* (2003) reported that the removing sun-glint can improve signal to noise ratio (SNR) of water depth estimation from 20:1 to 100:1. But study at areas of sun-glint is very important. First, estimation of amount of sun-glint could be used for retrieving atmospheric column of various gases (e.g., water

vapor and carbon dioxide) (Vespérini et al. 1999, Kleidman et al. 2000, Crisp et al. 2004). Second, Kaufman et al. (2002) reported that the sun-glint is needed for estimating aerosol absorption. In the past, method by adjustment of operational functionality was suggested to avoid glint-contamination (Khattak *et al.* 1991). The Sea-viewing Wide Field-of-view Sensor (SeaWiFS) has an operational functionality that tilts the sensor 20° away from nadir to avoid sun glint contamination (Zhang and Wang 2010). The Coastal Zone Colour Scanner (CZCS) sensor on Nimbus-7 has a function to adjust the tilt of the pitch axis sensor in the direction of the satellite in order to avoid sun-glint (Park *et al* 2005). However, these method is complicated and image distortion is serious. A computer capacity for data acquired from sensor that controlled by these method is 200 times larger than capacity required for correction of data obtained from satellite sensors that do not control the sun-glint effect (Kosik and Paci 1987). Various sun-glint correction method have been developed without control of sensor function. Sun-glint correction method can categorized as two (table 1). Method of the first category developed for open ocean imaging. And it estimate amount of glint is predicted from

statistical models of the sea surface using wind direction and speed, angle relative to sun and sensor position. But it is difficult to apply the first method because assumption of the monodirectionality of waves is not valid in the coastal area. So, separate set of methods was presented for coastal images. Some methods of removing sun-glint present for using reflectance data over ocean. Some methods categorized as first has limitation of strong sun-glint. Some methods categorized as second is required atmospheric correction before sun-glint correction. And this method is not appropriate for cloud detection because cloud detection is required to cover large area at the same time and quickly. And some methods categorized as second required cloud mask before sun-glint correction (Hochberg *et al.* 2003, Hedley *et al.* 2005, Lygenza *et al.* 2006). And the other method categorized as second have limitation about distortion of spectral information that is estimated lower than it actually at sun-glint affected pixel (Kutser *et al.* 2003).

Table 1 two concepts of the glint correction method, and it can be categorized by method principle

principle	Authors and References	target	limitation	Target resolution (m)
<p>Statistical models of the sea surface</p> <p>The amount of glint is predicted from wind direction and speed, angle relative to sun and sensor position</p>	<p>Cox and Munk (1954,1956)</p>	<p>Open water</p>	<p>Not valid for the brightest glint area</p> <p>Not valid for coastal and higher resolution</p>	<p>100-1,000</p>
<p>NIR band signal after atmospheric correction is due to sun-glint</p> <p>And it is proportion to the amount of VIS band signal.</p>	<p>Goodman et al(2008) Hochberg et al.(2003) Lyzenga et al(2006) Hedley et al.(2005)</p>	<p>Higher resolution coastal and aerial applications</p>	<p>Not valid for very shallow water (water depth is less than about 2m)</p>	<p>Less than about 10</p>

1.1.2. Cloud detection

Cloud detection is the primary step for using satellite data (He *et al.* 2011, SIMPSON *et al.* 2001). Especially, cloud-contaminated pixels over ocean are the error factors that can high influence on the accuracy of various ocean-based products that can contribute to understanding ocean circulation such as Sea Surface Temperature (SST), ocean color, and chlorophyll-a. These ocean based product help us to understand ocean circulation. In general, the cloud detection over ocean is known to be easier than over land because the surface type is constant. However, there are many difficulties with accurate cloud detection over the ocean. First, the variability of temperature due to ocean currents and seawater upwelling and the ocean-to-coast radiation contrast effect causes errors in cloud detection over ocean. Second, there is also a sun-glint phenomenon, should be consider as confounding factor for retrieval of ocean based product, due to the geometrical characteristics of the solar - sea surface - satellite, which does not appear over land. Third, the reflectance of geostationary orbit satellite has variations depending on satellite and solar

angle because geostationary orbit satellite is viewed from a particular location on Earth and have widely viewing angle. Therefore, when performing cloud detection over the ocean, it is necessary to detect the cloud considering the properties of the ocean. Many methods have been studied on oceanic cloud detection however most of method in the field such as Moderate Resolution Imaging Spectroradiometer (MODIS) and Advanced Himawari Imager (AHI) used static threshold method in order to simultaneously process a wide area. However, this static threshold method has difficulties in considering the properties of the ocean that changes with time and space (*An et al. 2005, Jeong et al, 2004*). And over ocean, threshold values depending on Solar Zenith Angle (SZA) or Viewing Zenith Angle (VZA) have been used (Saunders and Kriebel 1988, Karlsson 1996, Kärner and Girolamo 2001). This approach seems to take into account that reflectance and brightness temperature of cloud is affected by the solar angle and satellite angle. In this study, we suggest new cloud detection considering ocean spectral property such as sun-glint and variability of reflectance due to SZA and VZA. We collected the Himawari-8 / AHI reflectance a function of the SZA and VZA identified

as clear pixel by NOAA's AHI cloud product. The spectral library is used by applying the Dynamic Time Warping (DTW) to detect cloud pixels automatically.

1.1.3. Cloud detection in sun-glint

Commonly, cloud detection using visible channel is known as more difficult in areas of sun-glint (Bréon, and Henriot 2006, Saunders 1986, Platnick *et al.* 2003). Platnick *et al.* (2003) said that difficult situation arising in the detection of clouds from the water surface is the possibility of sun-glint observation. Clouds are generally characterized by higher reflectivities and lower brightness temperature. Clouds have same radiance as cloud-free sea surface in areas of sun-glint. So in case of sun-glint, simple threshold method are not effective (Saunders 1986). In practice, it was found that sun-glint caused cloud-free sea surface to be processed as clouds in large regions of tropics such as Indian Ocean (Platnick *et al.* 2003). A variety of sun-glint correction methods was presented and these methods can contribute to improve accuracy but is not commensurate with removing cloud pixels because most of sun-glint

correction methods requires complex prior step such as atmospheric correction and optimization of variables for each sensor. And some sun-glint correction methods require cloud detection as prior step. Therefore, cloud detection methods for real-time processing system such as Visible–Infrared Imager–Radiometer Suite (VIIRS) on the Suomi-National Polar-orbiting Partnership (S-NPP), MODIS on the Terra and Aqua, AHI on the Himawari-8 use the strict threshold value in areas of sun-glint contaminant. AHI cloud mask algorithm for Himawari-8 assigned sun-glint area using Cox and Munk models and use threshold value using reflectance ratio using $0.3.9 \mu\text{m}$ channel and $10.4 \mu\text{m}$ channel (Imai and Yoshida 2016). And VIIRS and MODIS cloud mask algorithm assigned areas of potential geometric sun-glint using geolocation of sun - sea surface – sensor.

2. Data and Materials

2.1. Himawari-8/AHI

In this study, we use the Himawari-8 data, the next generation meteorological geostationary orbit satellite of the Japan Meteorological Agency (JMA). Himawari-8 was successfully launched on 17 October and reached at 140.7 degrees east. The AHI sensor on the Himawari-8 satellite has a total of 16 channels covering from the visible bands to the thermal-infrared bands (0.46 μm ~13.3 μm). And their spatial resolution is from 0.5~2 km, 0.5km for 0.64 μm visible band, 1 km for visible and near-infrared bands, 2 km for infrared bands. AHI scan the Full Disk (FD) every 10 min and sectored regions every 2.5 min. The AHI has many new advantages than the previous generation satellite, Multifunctional Transport Satellite - 2 (MTSAT-2) in higher spatial resolution, the increased number of spectral bands and faster imaging. In this study, we used the Himawari-8 FD channel data from March to October, 2016, and constructed a spectral library on the ocean surface of clear sky using 5

spectral bands: RGB and two near infra-red channels. The center wavelength between 0.47um and 13.3 um spatial resolution are as shown in Table 1.



Figure 1 Study area - full disk of himawari-8/AHI

Table 2 Himawari-8/AHI specifications

	Wave length (μm)	Band number	Central wave length (μm)	Spatial resolution (km)
<i>Visible</i>	0.47	1	0.47063	1
	0.51	2	0.51000	1
	0.64	3	0.63914	0.5
<i>Near-infrared</i>	0.86	4	0.85670	1
	1.6	5	1.6101	2
	2.3	6	2.2568	2
	3.9	7	3.8853	2
	6.2	8	6.2429	2
	6.9	9	6.9410	2
	7.3	10	7.3467	2
<i>Infrared</i>	8.6	11	8.5926	2
	9.6	12	9.6372	2
	10.4	13	10.4073	2
	11.2	14	11.2395	2
	12.4	15	12.3806	2
	13.3	16	13.2807	2

2.2. Cloud mask of NOAA

It is very important to collect the spectral properties of pixels without any cloud effect when building the spectral library. Therefore, the AHI SST data of National Oceanic and Atmospheric Administration Advanced Clear-Sky Processor for Oceans (NOAA ACSPO) SST system were used. AHI SST has been validated with in-situ data through NOAA's in-situ SST Quality Monitor (iQuam) validation system and validated during eight days from July 15 ~ 22, 2015 to within the deviation of ± 0.2 K, within the standard deviation of 0.4~0.6 K was obtained. Cloud-contaminated pixels is one of the biggest error factors contributing to SST retrieval. So high accuracy of SST retrieval can represent high accuracy of cloud mask. The Quality flag of the AHI SST derived from the ACSPO SST system consists of a cloud, a probably cloud, and a clear. To collect the ocean surface reflectance without influence of cloud we used clear pixel to build ocean surface spectral library. And also, we used cloud mask of NOAA to compare with our result of cloud detection.

2.3. JMA cloud type data

The AHI cloud type data provided by the Japan Meteorological Agency (JMA) was used to verify the accuracy of the cloud detection. A spatial resolution of JMA cloud type data is 5km and time resolution of JMA cloud type data is 10min, day-time only. The Area of coverage is Lat. 60°S ~ 60°N and Lon. 80°E~200E°. The AHI cloud type data are divided into 10 types according to the International Satellite Cloud Climatology Project (ISCCP), including the clear and unknown (Table 2). We used JMA cloud type data for qualitative validation.

Table 3 JMA cloud type (ISCCP Definition)

FLAG	CLOUD TYPE(ISCCP)
0	Clear
1	Cirrus
2	Cirro-stratus
3	Deep convection
4	Alto-Cumulus
5	Alto-stratus
6	Nimbo-stratus
7	Cumulus
8	Strato-cumulus
9	Stratus
10	Unknown
255	Fill value

3. Methodology and Results

3.1. Synthetic Methodology

Before the cloud detection, we performed the construction of ocean surface spectral library. First, we performed reflectance normalization of AHI channel 1~5 using cosine of solar zenith angle. To collect the pixel where not affected by cloud, we selected and collected reflectance of AHI channel 1~5 only for clear pixel and the clear pixel is determined by AHI cloud mask of NOAA. And we detected cloud for daytime ($SZA < 80^\circ$), ocean and sun-glint region. And we adjusted dynamic threshold method, dynamic wavelength warping and IST_0 to determine clear pixel.

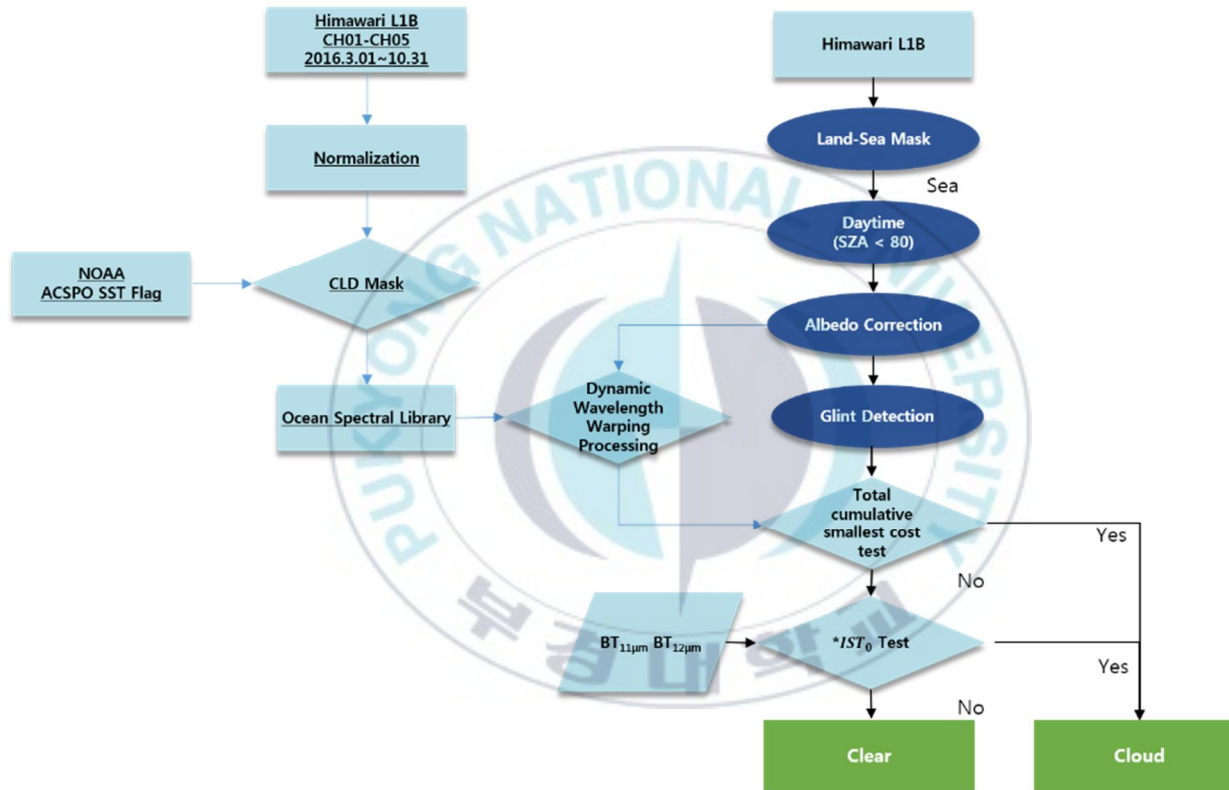


Figure 2 flow chart of this study

3.2. Reflectance Normalization

Reflectance at visible channel is strongly influenced by Solar Zenith Angle, and as SZA is the higher (i.e., small solar elevations), visible reflectance is the lower (schaaf and Strahler 1993). Therefore, reflectance at visible channel is necessary to correcting SZA effect. Reflectance (channel 1~5) was corrected by dividing the cosine of the solar zenith angle. And a portion of raw pixels reflectance is outside of the valid range that exceeds 1 by solar geometry effect. The resulting of albedo correction is adjusted within the valid range (0~1) (Simpson and Gobat 1995).

3.3. Sun-glint detection

3.3.1. Sun-glint detection

In this study, we used formula of sun-glint area suggested by Levy et al (2003). The sun-glint affected region can be calculated as a function of solar and sensor geometry. Levy et al suggested the sun-glint region using glint angle. Glint angle is formed between the sensor and solar specular reflection vectors. Glint angle defines as:

$\theta_{glint} = \cos^{-1}(\cos(SZA) \cos(VZA) - \sin(SZA) \sin(VZA) \cos(RAA))$	(1)
---	-----

where SZA, VZA, RAA are solar zenith angle, the satellite zenith angle and the relative azimuth angle respectively. We detect sun-glint area where glint angle is less than 40°.

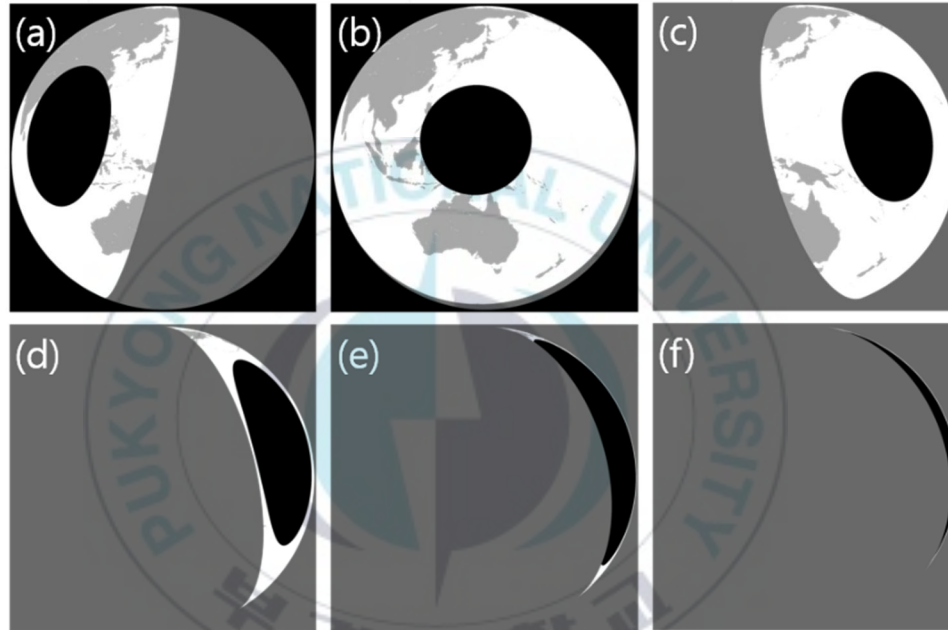


Figure 3 Sun-glint area in AH1's full disk disk as a function of glint angle(θ_g) and the threshold value is 40° (a) 2016/08/17 08:00 UTC (b) 2016/08/17 03:00 UTC (c) 2016/08/17 21:00 UTC (d) 2016/08/17 19:00 UTC (e) 2016/08/17 18:00 UTC (f) 2016/08/17 17:00 UTC

3.4. Construction of ocean spectral reflectance library

Cloud has a wide range of spectral reflectance characteristics depending on cloud type because type of cloud vary based on determined condensation level, shape, texture, composition and so on. Because of variability of spectral reflectance characteristics of cloud, detecting cloud of all type of cloud is thoroughly difficult, especially thin clouds. But spectral reflectance characteristics of cloud-free ocean is relatively constant in comparison with cloud. And ocean surface reflectance is sensitive to geophysical parameters: SZA, wind speed, transmission between cloud and aerosol and ocean chlorophyll concentration. (A parameterization of ocean surface albedo). And in breon (1993) study, the ocean surface albedo showed almost sixfold increase as solar zenith angle increase from 0 to 70 and only small relative change in ocean surface albedo by changing wind speed between 8 m/s and 14 m/s . This study showed that ocean surface reflectance is strongly influenced by solar zenith angle, more than other elements.

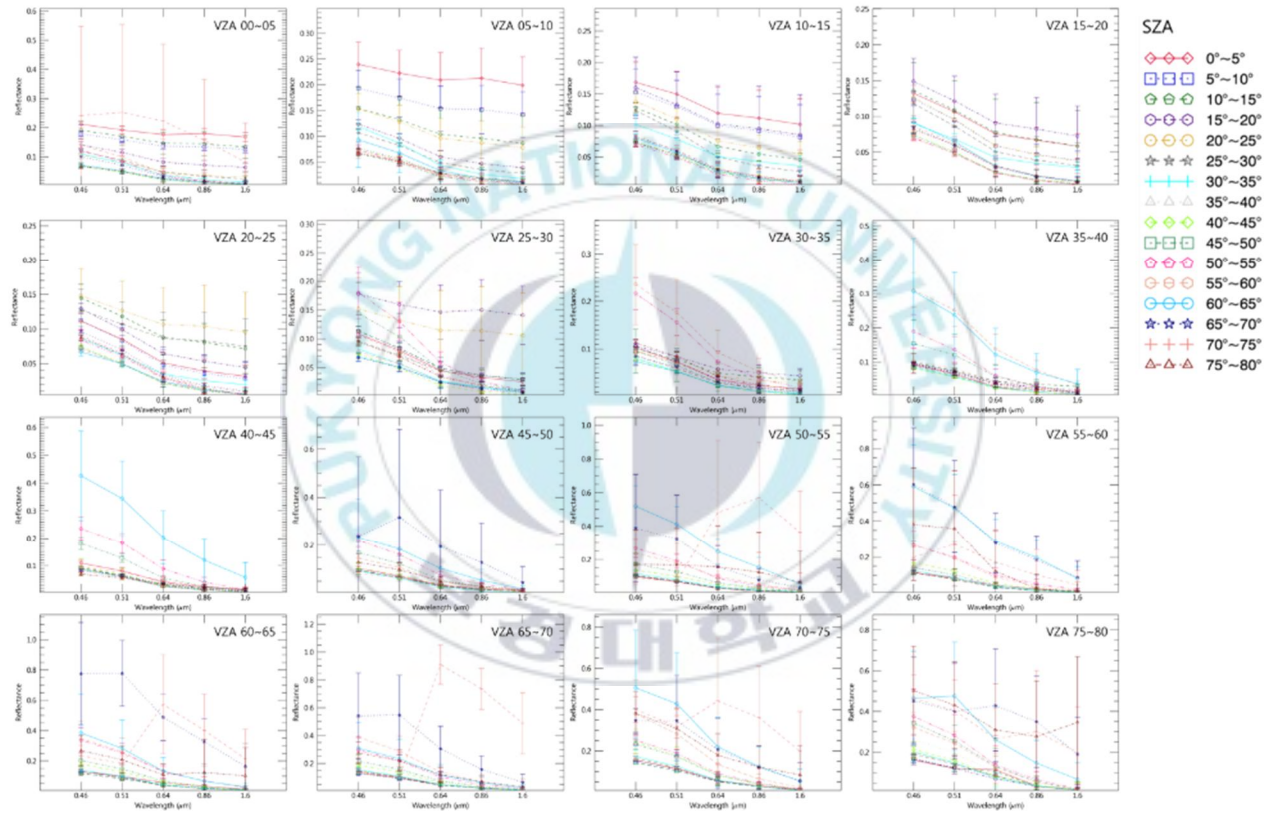


Figure 4 ocean spectral reflectance library depending change of SZA and VZA

So in this study, we collect spectral reflectance library of cloud-free ocean according to the change of SZA and VZA at an interval of 5° . Figure 4 is the result of construction of ocean surface spectral library in the visible and NIR wavelength range ($0.46 \sim 1.6 \mu\text{m}$). Figure 4 shows that ocean surface have a spectral characteristic that varies depending on SZA and VZA. But variability of range of values exist, but reflectance in the visible and NIR wavelength range ($0.46 \sim 1.6 \mu\text{m}$) over ocean has consistent pattern as SZA and VZA change. But these pattern is not constant at high SZA of $70\sim 80^\circ$. This tendency seems to be the cause of accuracy of quality flag of NOAA is low at high SZA because the number of clear pixel of quality flag of NOAA is small because quality flag of NOAA have a tendency of detect a large percentage of pixels as cloud at high SZA.

3.5. Dynamic Wavelength Warping (DWW)

3.5.1. Dynamic Time Warping (DTW)

Dynamic Time Warping (DTW) method was presented for improving the problem caused by changing the length of the voice even if the same

speaker pronounces the same word in automatic speech recognition by Hiroaki and Seibi in 1978. DTW method is kind of dynamic programming and it can recognize similarity between two sequences of two time series data even if they are out of phase. Because of this flexibility, DTW is used in many different fields including science, medicine, industry and finance (Keogh and Chotirat, 2005). DTW can be applied to any data that can be represented a linear sequence. Lee et al (2017) suggest DWW (Dynamic Wavelength Warping) applying DTW. DWW is the method to use wavelength data, not time series data. DTW method measure similarity based on Euclidean distance. Euclidean distance is commonly accepting the method that measure simplest distance between two time series data. Suppose there are two time series, A and B, of length n and m respectively.

$A = a_1, a_2, a_3, \dots, a_i, \dots, a_n$	(2)
---	-----

$B = b_1, b_2, b_3, \dots, b_i, \dots, b_n$	(3)
---	-----

And before the use DTW, we construct an n-by-m matrix where contains the Euclidean distance, (i^{th}, j^{th}) . And The Euclidean distance between A and B is defined by equation (2) and equation (3).

$d(a_i, b_j) = \sqrt{(a_i - b_j)^2}$	(4)
--------------------------------------	-----

DTW method is to find warping path that is defined a mapping between A and B that minimum of warping cost. And the warping cost is defined as the distance between two sequences when the path is optimal aligned. And optimal alignment can be computed by

$\gamma(i,j) = d(a_i, b_j) + \min\{ \gamma(i-1,j-1), \gamma(i-1,j), \gamma(i,j-1) \}$	(5)
---	-----

$\gamma(i,j)$ is the i^{th}, j^{th} value in warping path consisting minimum of the cumulative distances of the adjacent elements ($i - 1^{th}, j - 1^{th}, i - 1^{th}, j^{th}, i^{th}, j - 1^{th}$).

3.5.2. Dynamic Wavelength Warping (DWW)

Dynamic Wavelength Warping (DWW) method is presented by Lee et al (2017). Lee used the two wavelength data, one is constructed spectral library and one is observed reflectance, instead of two time serious data and determined similarity between two wavelength data. And Lee performed cloud-snow discrimination if the line of warping path is diagonal. And Lee et al executed successfully cloud-snow discrimination compared with MODIS snow cover. Especially at high VZA, MODIS snow cover algorithm was a tendency to detect snow as cloud, but DWW was a tendency to detect snow as snow.

In this study, given the characteristics that the variability of the ocean is less than the cloud, we construct spectral library at cloud-free ocean surface instead of cloud spectral library. Ocean surface spectral library was construct as a function of SZA and VZA. DWW method was used to discriminate cloud and ocean using the total cumulative smallest cost.



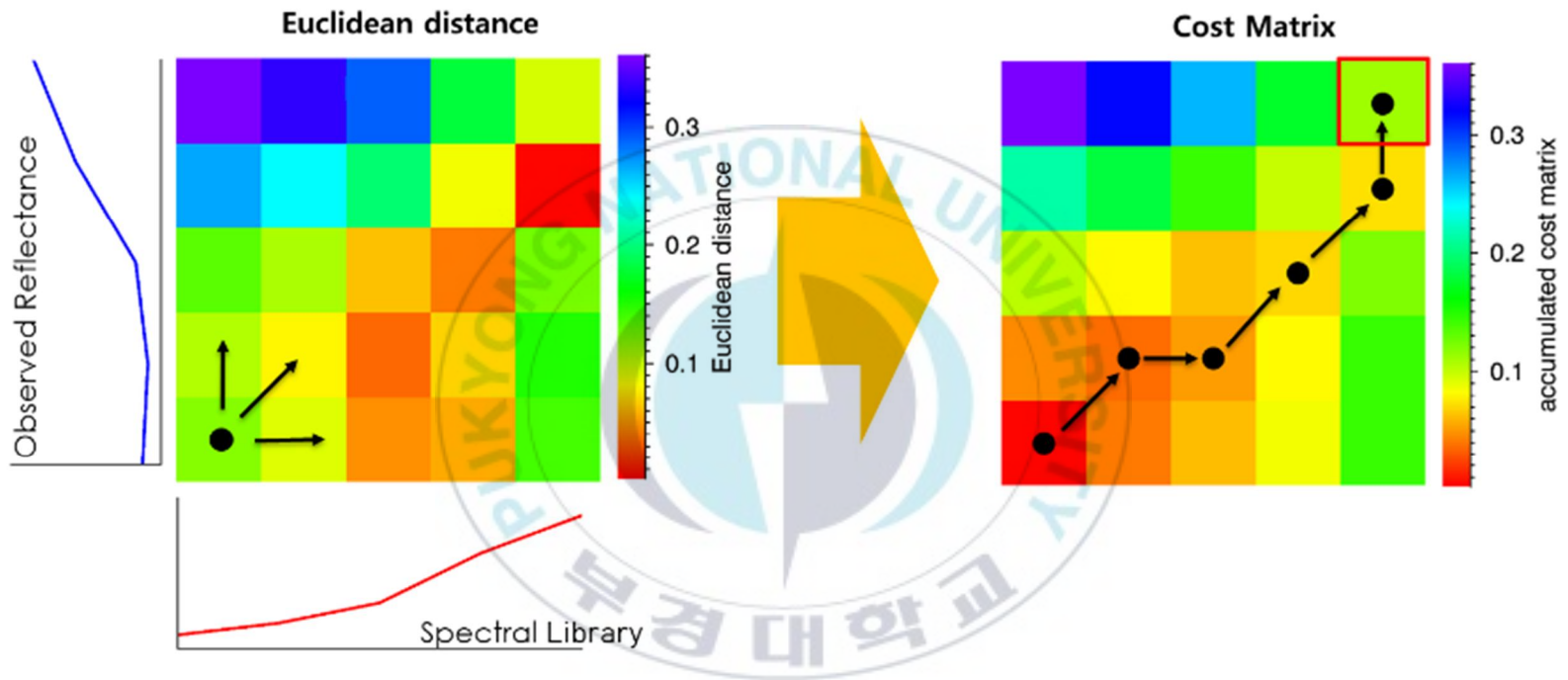


Figure 5 To find the optimal warping path, we construct a Cost matrix using Dynamic Time Warping (DTW) method

3.6. IST_0 method

Reflectance at AHI channel 1~5 in NOAA's clear pixels showed a tendency to have high values at sun-glinton area and solar zenith angle larger than 80° and it can lead to be misinterpreted as cloud pixels, so we used IST_0 calculated from the $10.4\ \mu\text{m}$ band and $11.2\ \mu\text{m}$ band to redeem an error caused by sun-glinton error and solar zenith angle. Jin et al (2017) found the linear relationship between ice surface temperature, $11.03\ \mu\text{m}$ brightness temperature and differences between $11.03\ \mu\text{m}$ and $12.02\ \mu\text{m}$ brightness temperature of MODIS when temperature of seawater is lower than the freezing point of seawater. Using this linear relationship, Jin et al (2017) performed IST_0 retrieval, $11.03\ \mu\text{m}$ brightness temperature of MODIS when ice surface temperature of MODIS is $273.0\ \text{K}$ corresponding these linear relationship. IST_0 was used for sea ice detection by taking advantage of the fact that brightness temperature of sea ice lower than sea. When we use the IST_0 to cloud detection, the biggest concerns is confounding of sea ice and cloud because both sea ice and cloud are lower than ocean surface. So we compare with spatial distribution of sun-glinton area during $00:00 \sim 23:00$ UTC on August first, 2016 and cumulated spatial distribution of weekly

sea ice of National Snow and Ice Data Center (NSIDC) during Northern hemisphere winter season (from December to February) from 1980 to 2015. Result of comparison of two distribution area, sea ice was rarely observed in sun-glint area from 1980 to 2015. So, IST_0 can be method for cloud detection over ocean within an area of sun-glint.

IST_0 was determined as follows equation.

$IST_0 = A * (BT_{11.03\mu m} - BT_{12.02\mu m}) + B$	(6)
---	-----

When A is -2.056, B is 273.1, $BT_{11.03\mu m}$ is Brightness temperature of $11.03\mu m$ of MODIS, $BT_{12.02\mu m}$ is brightness temperature of $12.02\mu m$ of MODIS.

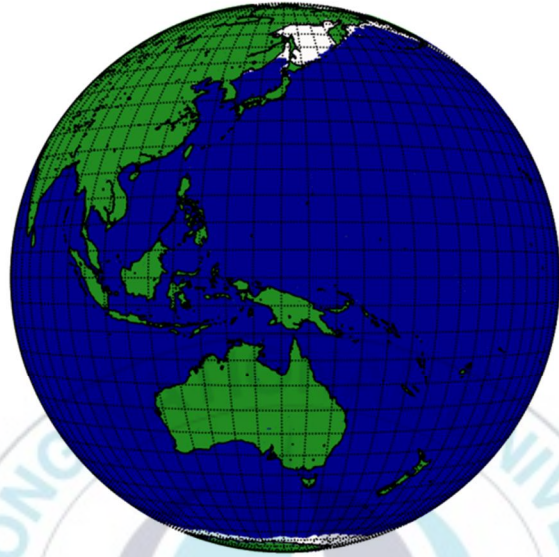


Figure 6 spatial distribution of weekly sea ice of National Snow and Ice Data Center (NSIDC) during Northern hemisphere winter season (from December to February) from 1980 to 2015

4. Evaluation

4.1. Evaluation of result of cloud detection using DWW

Figure 7 (a) shows the total cumulative smallest cost value, Figure 7 (b) shows red-green-blue (RGB) composite image and Figure 7 (c) shows area that total cumulative smallest cost value larger than 0.6 at region of sun-glint for the 03:00 UTC on August 1, 2016. Total cumulative smallest cost value is the last value of the cost matrix and it means similarity between two patterns, reflectance profile observed and selected reflectance profile from ocean spectral reflectance library according to SZA and VZA at the time of observation. The meaning of red circle in Figure 7 (b) is glinted area on RGB composite image. As shown in Figure 7 (a) and (b), although glinted area caused by sun-glint effect, total cumulative smallest cost value is less than cloud area on RGB composite image. As shown in Figure 7 (b) and (c), we set threshold of total cumulative smallest cost value of 0.6 and the shape of result of cloud detection is similar with cloud shape of RGB composite image.

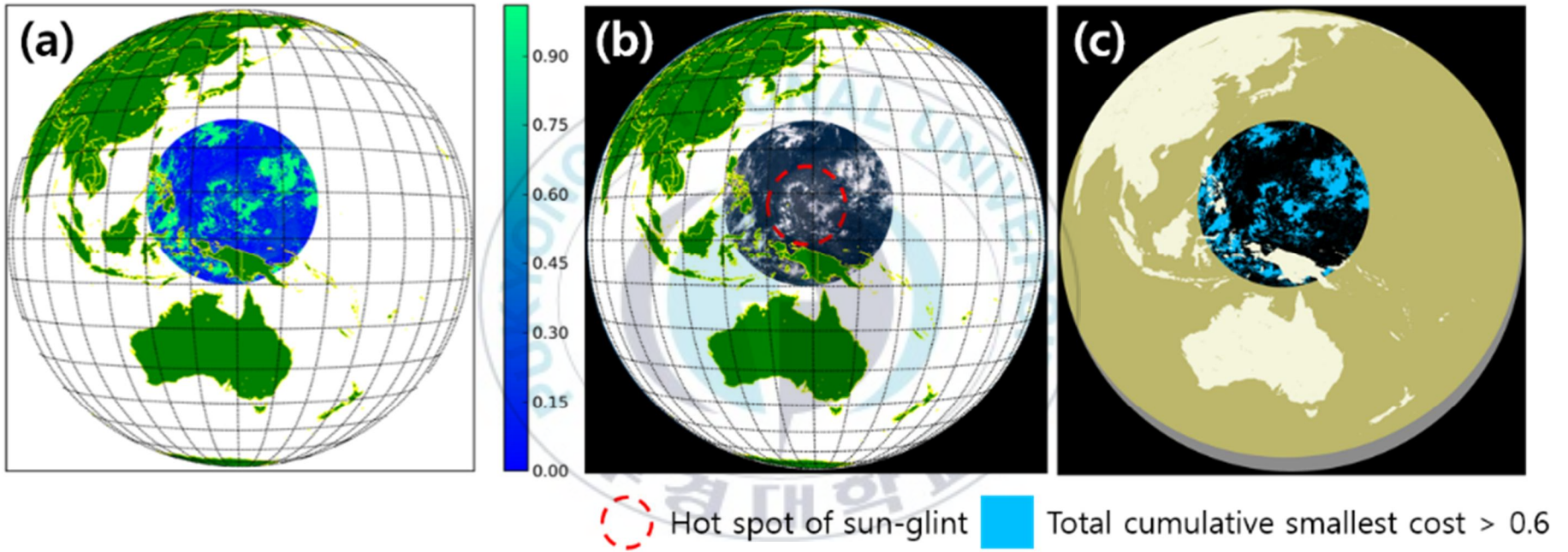
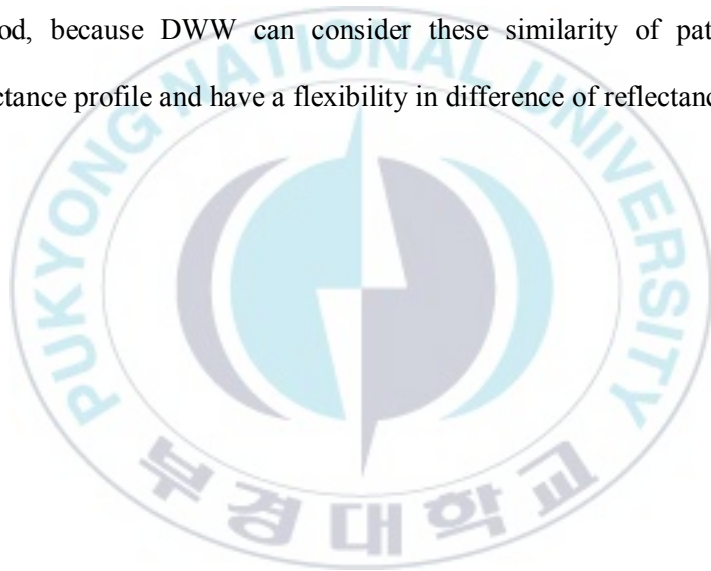


Figure 7 (a) is total cumulative smallest cost value, (b) is red-green-blue (RGB) composite image and (c) is detected area that total cumulative smallest cost value larger than 0.6 at region of sun-glint acquired at 03:00 UTC 1 August 2016

We select the three pixels to figure out ability of DWW under the different condition pixels that one in clear and no glinted (Figure 8(a)), another in cloud and no glinted (Figure 8(b)), the other in clear and glinted (Figure 8(c)). We assigned three pixels case 1, case 2 and case 3 respectively (see Table 1). We assigned Figure 8(a) as case 1 and it was classified as cloud by AHI SST quality flag of NOAA, cloud type of JMA, result of our study and eyeball comparison of RGB composite image. We assigned Figure 8(b) as case 2 and it was classified as clear by AHI SST quality flag of NOAA, cloud type of JMA, result of our study and eyeball comparison of RGB composite image. We assigned Figure 8(c) as case 3 and it was classified as cloud by AHI SST quality flag of NOAA and cloud type of JMA, but it was classified as clear by result of our study and eyeball comparison of RGB composite image. In case 2, two pattern of reflectance profile observed and selected reflectance profile from ocean spectral reflectance library is similar by comparison with case 1. Because the total cumulative smallest cost reflected the similarity, the total cumulative smallest cost of case 2 was smaller than case 1. In case 1 and case 2, these pixels were classified as cloud and clear pixel unaffected sun-glint in qualitative comparison of RGB composite image and it can be easily detected and not ruled out as cloud. In case 2 and case 3, the pixels were classified as clear in qualitative comparison of RGB composite

image, but the reflectance in case 3 is higher than ocean spectral reflectance library by comparison with reflectance in case 2. In case 3, the reflectance measures high, but the pattern of reflectance profile observed and selected reflectance profile from ocean spectral reflectance library is similar by comparison with pattern in case 1. The pixels affected by sun-glint can be discriminate between clear sky and cloud by using DWW method, because DWW can consider these similarity of pattern of reflectance profile and have a flexibility in difference of reflectance.



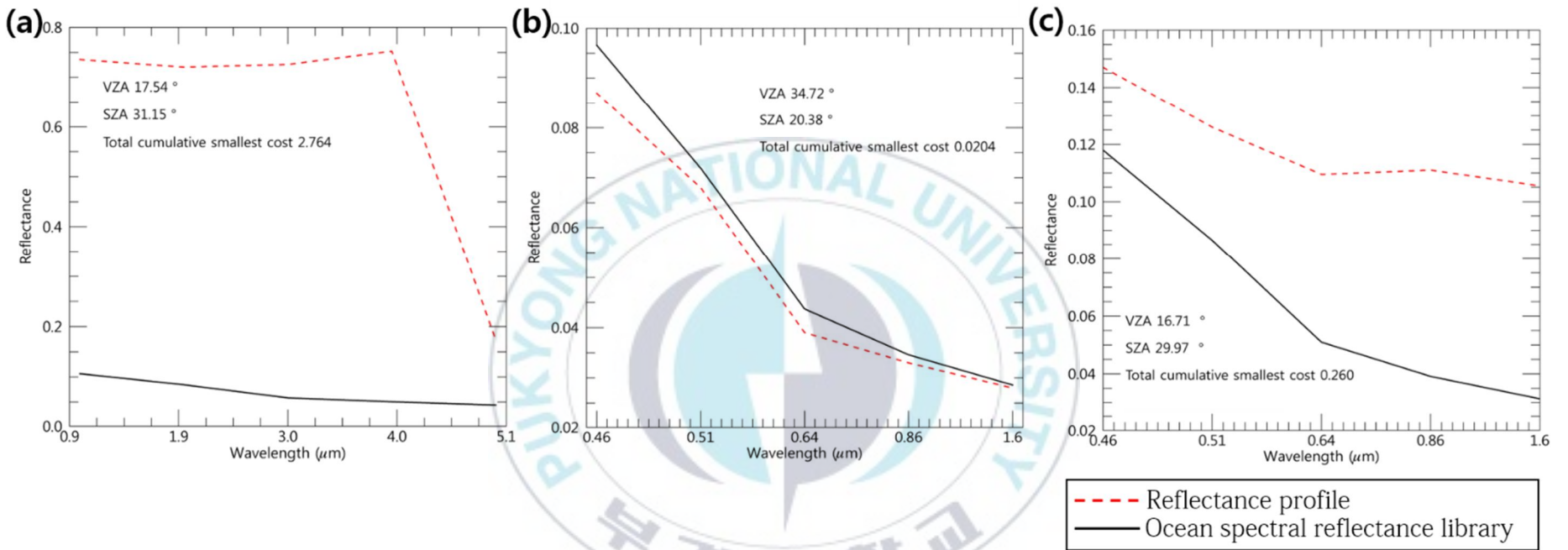


Figure 8 plotted reflectance profile observed and selected reflectance profile from ocean spectral reflectance library under SZA and VZA condition at the time of observation

Table 4 Case classification of RGB true color image and cloud mask from NOAA, JMA and our result

	NOAA	JMA	Our result	RGB
<i>Case 1</i>	Cloud	Cloud (Deep convection)	Cloud	Cloud
<i>Case 2</i>	Clear	Clear	Clear	Clear
<i>Case 3</i>	Cloud	Cloud (Stratocumulus)	Clear	Clear

Table 5 Information about SZA, VZA, Total cumulative smallest cost in each case

	Case 1	Case 2	Case 3
<i>SZA (degree)</i>	31.15	20.38	29.97
<i>VZA (degree)</i>	17.54	34.72	16.71
<i>Total cumulative smallest cost</i>	2.764	0.0204	0.260

4.2. Evaluation of result of cloud detection using IST_0

Pixels located at thick clouds flagged by total cumulative smallest cost value test. Pixels located at outer border of cloud mostly flagged by IST_0 test where pixels is undetected by total cumulative smallest cost value test. Figure 9(a) shows that cloud detection result at 0300 UTC 1 August 2016. The sky blue indicates the pixels flagged as cloud by thresholding the value of total cumulative smallest cost value greater than 0.6. The orange indicates the pixels flagged as cloud by thresholding the value of difference between IST_0 and $11.2 \mu\text{m}$ channel BT greater than -15K. IST_0 test was performed only for the pixels undetected by total cumulative smallest cost test. Black indicates clear and grey indicates where SZA is greater than 80° . Figure 9(b) shows a true color RGB image as an example of clouds and clear sky in the same scene. When comparing Figure 9(a) and Figure 9(b), distribution of cloud mask determined by IST_0 test is similar with distribution of cloud of the true color RGB image.

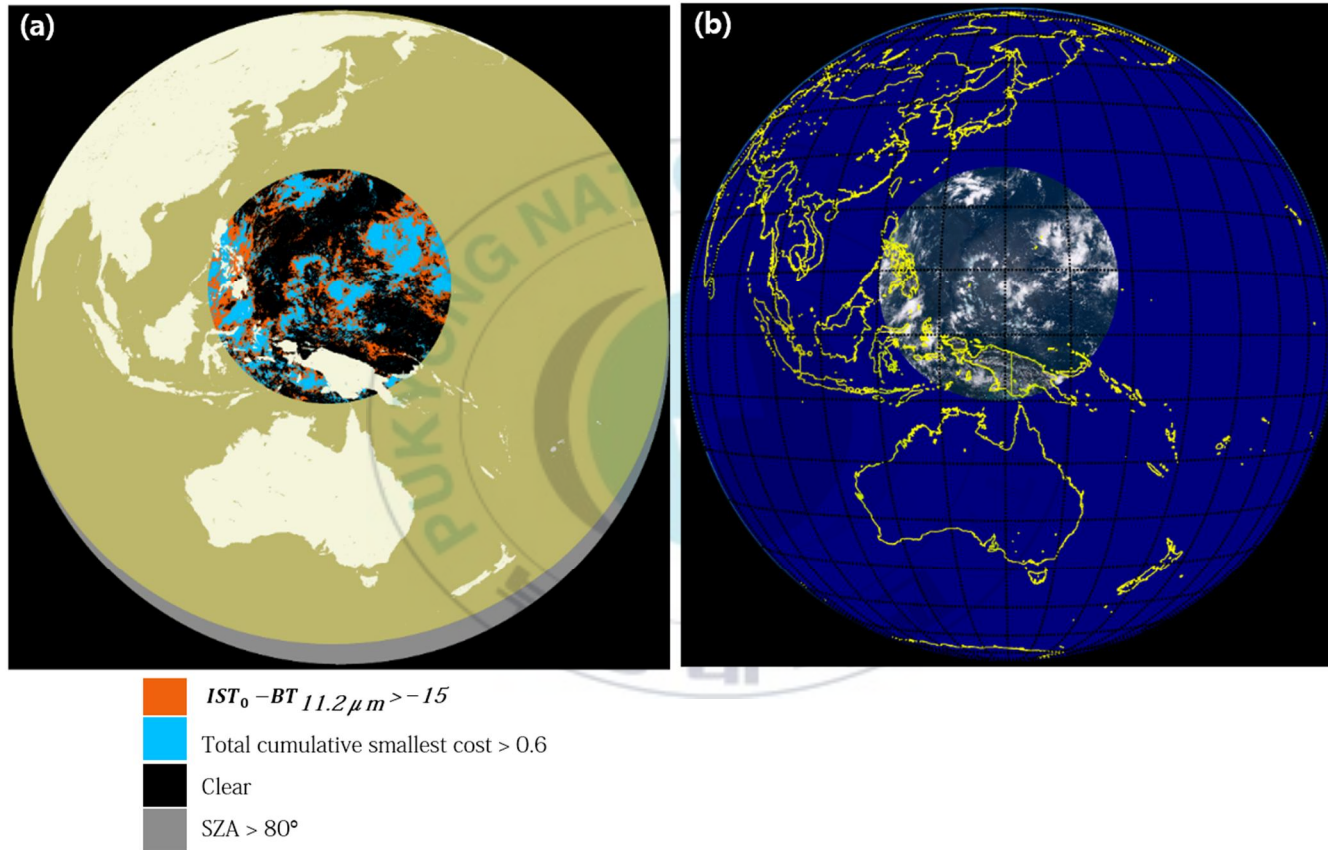


Figure 9. A case from 0300 UTC on 1 August 2016. (a) sky blue is cloud detection result when total cumulative smallest cost is greater than 0.6 and orange is cloud detection result when $IST_0 - 11.2\ \mu m$ channel BT is greater than -15 K (b) RGB composite image

4.3. Qualitative validation with AHI cloud type of JMA and AHI SST quality flag of NOAA

We accomplished qualitative validation with quality flag of AHI SST of NOAA and AHI cloud type of JMA. Figure 10 shows qualitative validation with AHI cloud type of JMA and cloud detection result of this study. Figure 10(a) shows true color RGB image at 0100 UTC 1 August 2016. Figure 10(b) AHI cloud type data of and Figure 10(c) cloud detection result JMA in the same scene. The red box indicates where area is strongly affected by sun-glint. Pixels in red box in Figure 10 classified as clear by visual comparison with RGB true color image As seen in Figure 10(b) and Figure 10(c), JMA classified these pixel as cloud, but the proposed algorithm categorized classified these pixel as clear. By comparison with Figure 10(b) and Figure 10(c), cloud detection algorithm of JMA has tendency to misclassified clear as cloud when sun-glint effect is strong, but proposed algorithm detects well most of these regions. Figure 11 shows visual comparison with true color RGB image, AHI SST quality flag of NOAA and our cloud detection result at 0100 UTC 1 August 2016. Figure 11 (a) shows true color RGB image, Figure 11 (b) shows AHI SST quality flag of NOAA and Figure 11 (c) shows cloud detection result at the same time. As seen in Figure 11 (a) and Figure 11(b),

NOAA cloud detection algorithm has a tendency to overestimate cloud by comparison with RGB image. As seen in Figure 11 (a) and Figure 11(c), cloud mask by proposed algorithm seen to similar distribution comparing with RGB image. Figure 12 (a) shows true color RGB image, Figure 12 (b) shows AHI cloud type of JMA and Figure 12 (c) shows cloud detection result at 0200 UTC 3 August 2016. As seen in Figure 12(a) and Figure 12(b), JMA has tendency to overestimate cloud when sun-glint effect is strong. However as seen in Figure 12(a) and Figure 12(c), cloud mask by proposed algorithm doesn't have tendency to overestimate cloud when sun-glint effect is strong. Cloud mask by proposed algorithm seem to have similar distribution with RGB image. Figure 13 (a) shows true color RGB image, Figure 13 (b) shows AHI SST quality flag of NOAA and Figure 13 (c) shows cloud detection result at 0200 UTC 3 August 2016. As seen in Figure 13(a) and Figure 13(b), NOAA tend to overestimate cloud where sun-glint affected area. However, as seen in Figure 13(a) and Figure 13(c), Cloud mask by proposed algorithm seem to have similar distribution with RGB image.

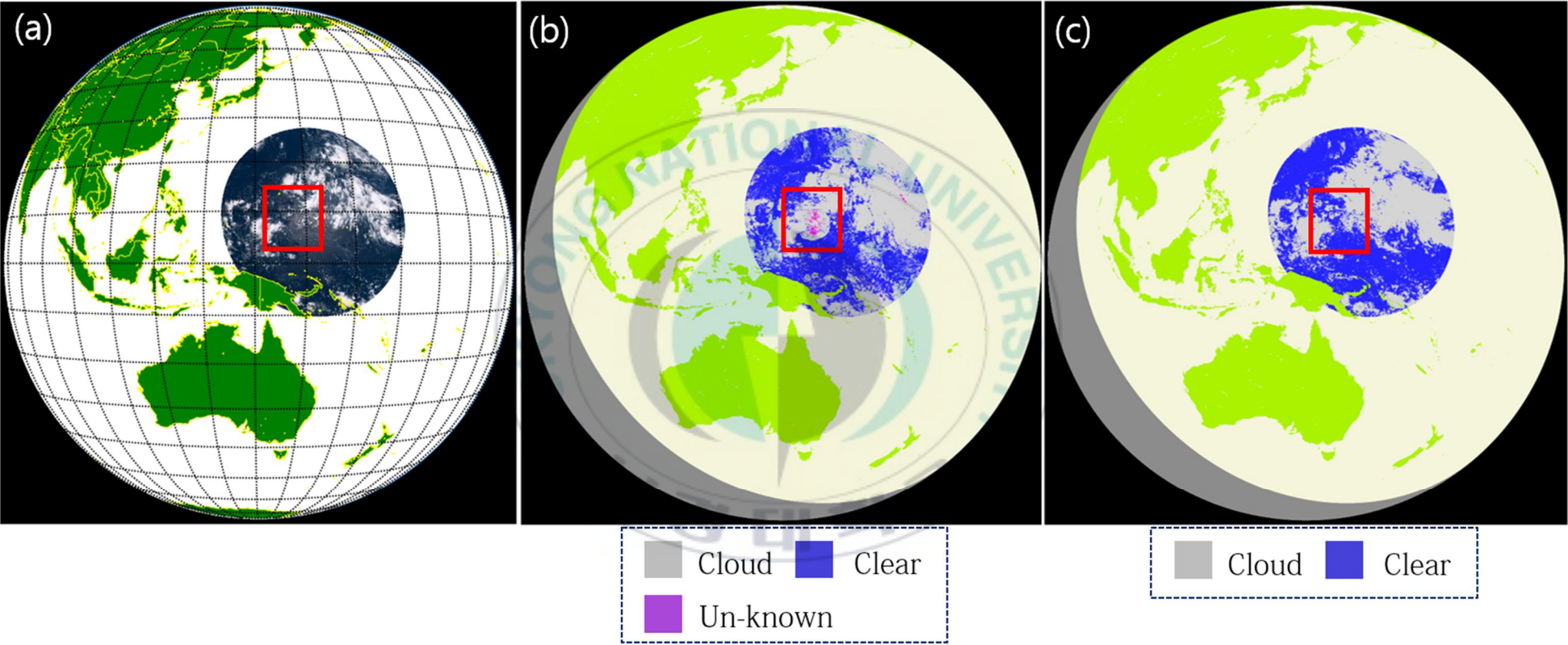


Figure 10 visual comparison with true color RGB image, AHI cloud type of JMA and our cloud detection result at 0100 UTC 1 August 2016

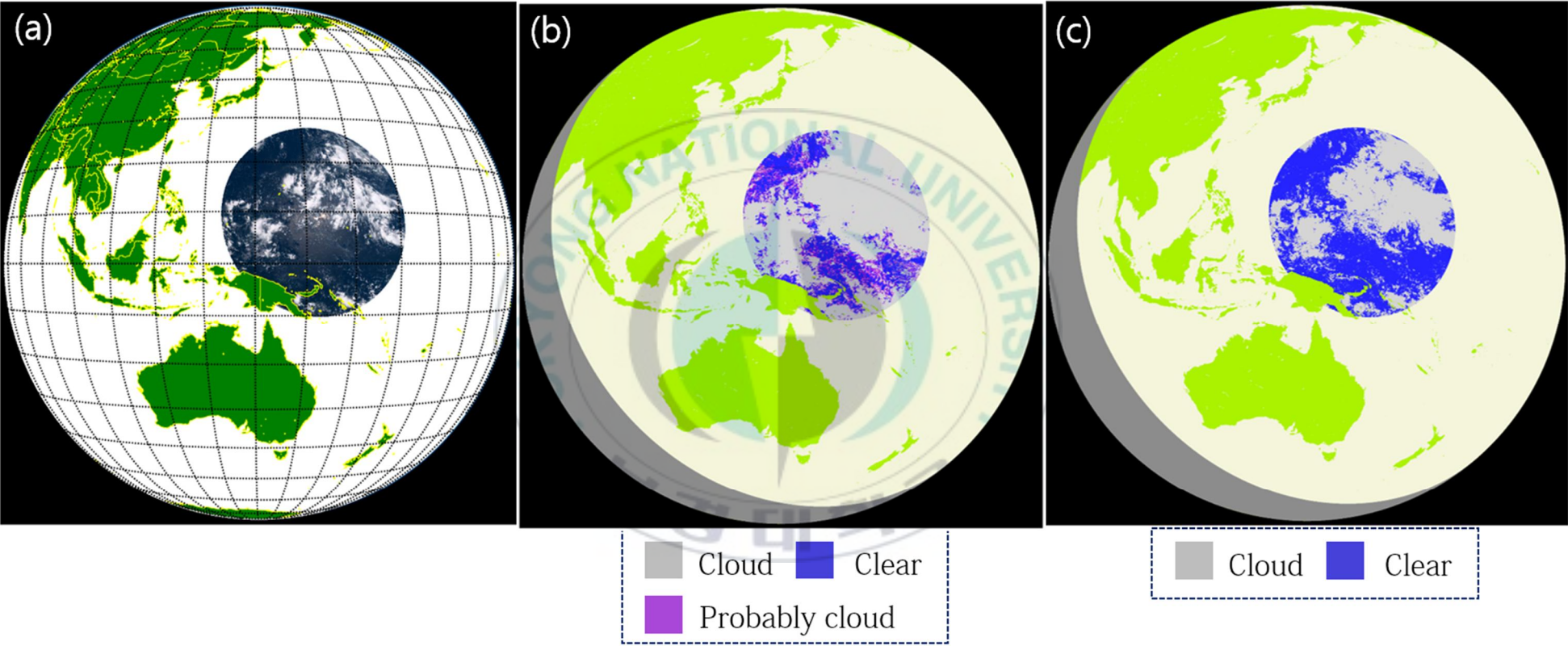


Figure 11 visual comparison with true color RGB image, AHI SST quality flag of NOAA and our cloud detection result at 0100 UTC 1 August 2016

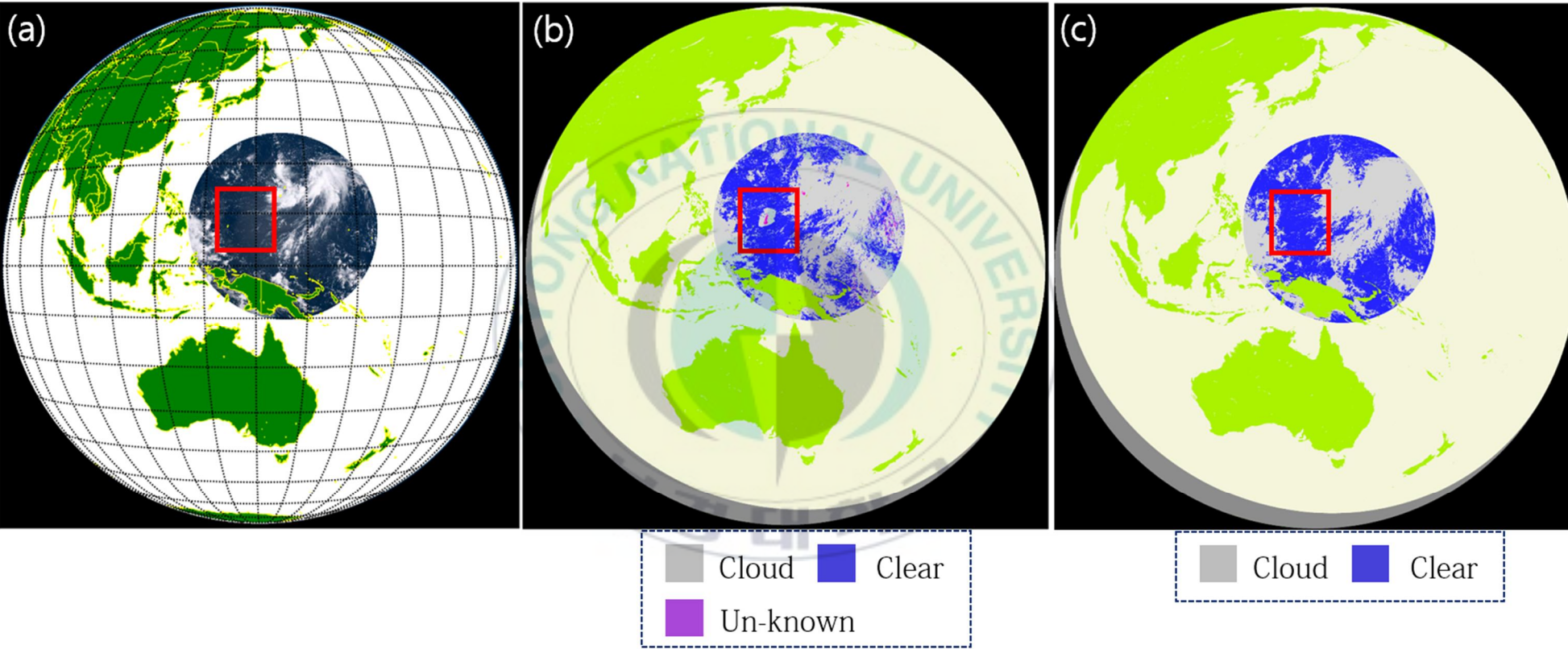


Figure 12 visual comparison with true color RGB image, AH1 cloud type of JMA and our cloud detection result at 0200 UTC 3 August 2016

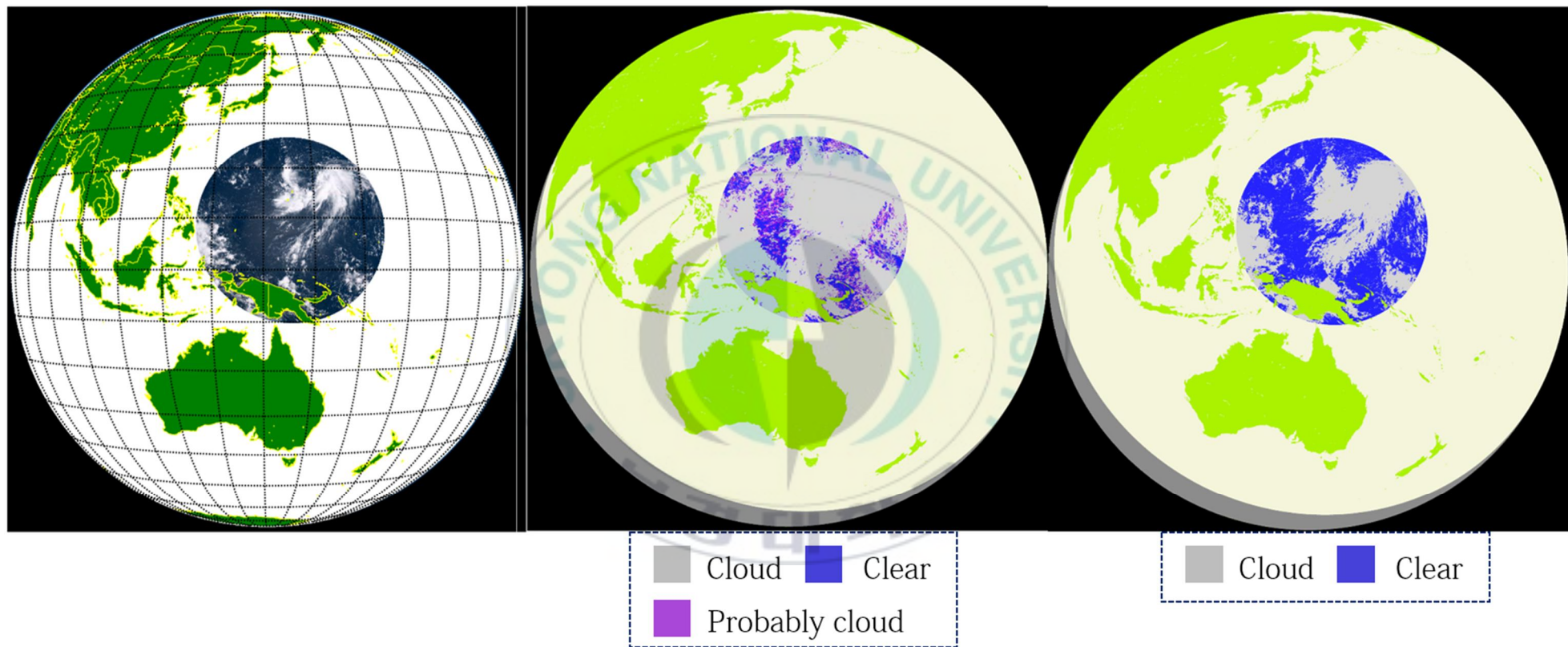


Figure 13 visual comparison with true color RGB image, AHI SST quality flag of NOAA and our cloud detection result at 0200 UTC 3 August 2016

5. Summary and Conclusions

In this study, we proposed a simple algorithm for cloud detection in sun-glint affected areas. Most cloud detection method use a static threshold because a static threshold has many advantage of cloud detection for large observation area and high time resolution. But static threshold method can't concern about spectral variability over ocean due to geometric relationship between sun, sea surface and sensor. And also, most cloud detection method use the cloud spectral properties. But because the cloud spectral properties vary depending various cloud properties for example cloud top height, cloud optical thickness and its component, considering of all spectral characteristic of cloud is difficult, so some clouds is difficult to detect such as thin cloud and low cloud. So in this study, we use spectral reflectance characteristic of cloud-free ocean instead of cloud because reflectance over ocean have few variability except variability due to geometric relationship between sun, sea surface and sensor.

6. References

- An, H.J., J.Y. Jeong, and M.H. An, 2005. Cloud detection in satellite imagery using neural network model, *Korean Meteorological Society*, **4**, 442-443 (in Korean).
- Bréon, F. M., 1993. An analytical model for the cloud-free atmosphere/ocean system reflectance. *Remote Sensing of Environment*, **43**(2), 179-192.
- Bréon, F. M., & Henriot, N., 2006. Spaceborne observations of ocean glint reflectance and modeling of wave slope distributions. *Journal of Geophysical Research: Oceans*, **111**(C6).
- Cox, C., and Munk, W., 1954. Measurement of the roughness of the sea surface from photographs of the sun's glitter. *JOSA*, **44**(11), 838-850.
- Cox, C., and Munk, W., 1956. Slopes of the sea surface deduced from photographs of sun glitter. *Scripps Institution of Oceanography*.
- Hochberg, E. J., Andrefouet, S., and Tyler, M. R., 2003. Sea surface correction of high spatial resolution Ikonos images to improve bottom mapping in near-shore environments. *IEEE transactions on geoscience and remote sensing*, **41**(7), 1724-1729.
- Hedley, J. D., Harborne, A. R., and Mumby, P. J., 2005. Simple and robust removal of sun glint for mapping shallow-water benthos. *International Journal of Remote Sensing*, **26**(10), 2107-2112.
- He, Q. J., 2011. A daytime cloud detection algorithm for FY-3A/VIRR data. *International Journal of Remote Sensing*, **32**(21), 6811-6822.
- Imai, T., and Yoshida, R., 2016. Algorithm theoretical basis for Himawari-8 Cloud Mask Product. *Meteorol. Satell. Center Tech. Note*, **61**, 1-17.
- Ignatov, A., P. Minnis, N. Loeb, B. Wielicki, W. Miller, S. Sun-Mack, D. Tanré, L. Remer, I. Laszlo, and E. Geie., 2005. Two MODIS aerosol

- products over ocean on the Terra and Aqua CERES SSF datasets. *Journal of the atmospheric sciences*, **62**(4), 1008-1031.
- Jeong C., 1997. Korean speech recognition, *The Magazine of the IEK*, **24**(9), 1071-1078 (in Korean).
- Jin, D., Lee, K. S., Choi, S., Seo, M., Lee, D., Kwon, C.Y., and Han, K. S. (2017). Determination of dynamic threshold for sea-ice detection through relationship between 11 mu m brightness temperature and 11-12 mu m brightness temperature difference. *KOREAN JOURNAL OF REMOTE SENSING*, **33**(2), 243-248.
- Kay, S., Hedley, J. D., and Lavender, S., 2009, Sun glint correction of high and low spatial resolution images of aquatic scenes: a review of methods for visible and near-infrared wavelengths. *Remote Sensing*, **1**(4), 697-730.
- Kutser, T., Dekker, A. G., and Skirving, W., 2003. Modeling spectral discrimination of Great Barrier Reef benthic communities by remote sensing instruments. *Limnology and Oceanography*, **48**(1part2), 497-510.
- Khattak, S., Vaughan, R. A., and Cracknell, A. P., 1991. Sun glint and its observation in AVHRR data. *Remote Sensing of Environment*, **37**(2), 101-116.
- Kosik, J. C., and Paci, G., 1981. Particular features of the ocean glitter pattern observed from a sun-synchronous orbit. *International Journal of Remote Sensing*, **2**(3), 265-275.
- Kutser, T., A.G. Dekker and W. Skirving., 2003. Modeling spectral discrimination of Great Barrier Reef benthic communities by remote sensing instruments. *Limnology and Oceanography* 48:497-510.
- Kärner, O., and Di Girolamo, L. (2001). On automatic cloud detection over ocean. *International Journal of Remote Sensing*, **22**(15), 3047-3052.
- Karlsson, K. G., 1996. Cloud classifications with the SCANDIA model. SMHI.

- Lee, K. S., Jin, D., Yeom, J. M., Seo, M., Choi, S., Kim, J. J., & Han, K. S., 2017. New Approach for Snow Cover Detection through Spectral Pattern Recognition with MODIS Data. *Journal of Sensors*, **2017**.
- Levy, R. C., Remer, L. A., Tanré, D., Kaufman, Y. J., Ichoku, C., Holben, B. N., ... and Maring, H., 2003. Evaluation of the Moderate-Resolution Imaging Spectroradiometer (MODIS) retrievals of dust aerosol over the ocean during PRIDE. *Journal of Geophysical Research: Atmospheres*, **108**(D19).
- Lyzenga, D. R., Malinas, N. P., and Tanis, F. J., 2006. Multispectral bathymetry using a simple physically based algorithm. *IEEE Transactions on Geoscience and Remote Sensing*, **44**(8), 2251-2259.
- OYOSHI, Kei; TAKEUCHI, Wataru; YASUOKA, Yoshifumi. Evaluation of snow-cover maps over Northeastern Asia derived from AVHRR, MODIS and MTSAT data. In: Proceedings of the 28th Asian Conference on Remote Sensing (ACRS). 12–16 November 2007, Kuala Lumpur, Malaysia. 2007.
- Park, J.I., Choi, K.H., Park, S.Y., Ryu, J.H., Ahn, Y.H., Park, J.W., and Kim, B.S., 2005. Prediction of the sun-glint location for the communication, ocean and meteorological satellite. *Journal of Astronomy and Space Science*, **22**(3), 263-272.
- Platnick, S., King, M. D., Ackerman, S. A., Menzel, W. P., Baum, B. A., Riédi, J. C., & Frey, R. A., 2003. The MODIS cloud products: Algorithms and examples from Terra. *IEEE Transactions on Geoscience and Remote Sensing*, **41**(2), 459-473.
- Sakoe, H., and Chiba, S., 1978. Dynamic programming algorithm optimization for spoken word recognition. *IEEE transactions on acoustics, speech, and signal processing*, **26**(1), 43-49.
- Saunders, R. W., 1986. An automated scheme for the removal of cloud contamination from AVHRR radiances over western Europe. *International Journal of Remote Sensing*, **7**(7), 867-886.

- Saunders, R. W., and Kriebel, K. T., 1988. An improved method for detecting clear sky and cloudy radiances from AVHRR data. *International Journal of Remote Sensing*, **9**(1), 123-150.
- Simpson, J. J., McIntire, T. J., Stitt, J. R., & Hufford, G. L. (2001). Improved cloud detection in AVHRR daytime and night-time scenes over the ocean. *International Journal of Remote Sensing*, **22**(13), 2585-2615.
- Schaaf, C. B., and Strahler, A. H., 1993. Solar zenith angle effects on forest canopy hemispherical reflectances calculated with a geometric-optical bidirectional reflectance model. *IEEE Transactions on Geoscience and Remote Sensing*, **31**(4), 921-927.
- Simpson, J. J., and Gobat, J. I., 1995. Improved cloud detection in GOES scenes over land. *Remote Sensing of Environment*, **52**(1), 36-54.
- Wang, M., & Bailey, S. W. (2001). Correction of sun glint contamination on the SeaWiFS ocean and atmosphere products. *Applied Optics*, **40**(27), 4790-4798.
- Zhang, H., and Wang, M., 2010. Evaluation of sun glint models using MODIS measurements. *Journal of Quantitative Spectroscopy and Radiative Transfer*, **111**(3), 492-506.